Synergy between asymmetric contact geometry and self-powered operation of an ultrasensitive CsPbBr$_3$ photodetector

Sandaap Sathyanarayana, Navaneeth Krishnan K⬤, and Bikas C. Das⬤[*]

eNDR Laboratory, School of Physics, IISER Thiruvananthapuram, Vithura, Trivandrum 695551, Kerala, India

High-performance self-powered photodetectors are in high demand for many applications in wireless sensor networks, Internet-of-things devices, wearable electronics, optical communication, and biomedical sensing. The self-powered photodetector design requires a type-II staggered heterojunction between two semiconductors. Hence, conventional heterojunction-free self-powered photodetector designs remain a challenging task. Here, we report a self-powered photodetector of significantly high performance using an all-inorganic CsPbBr$_3$ monocrystal grown *in situ* directly over the substrate with prepatterned interdigitated gold (Au) electrodes. Interestingly, we achieved an extremely low dark current of about 1 fA at room temperature, a dark-to-light current ratio of 10^7, a responsivity of 2 A/W, and a specific detectivity of 10^{14} Jones in self-powered mode. The self-powered nature of the Au/CsPbBr$_3$/Au photodetector with asymmetric contact geometry is investigated theoretically using a back-to-back Schottky diode model and experimentally using the Kelvin-probe force microscopy technique. Both approaches converged to predict the existence of a sufficient contact potential difference between the metal contacts due to having an interfacial area difference, which remains the source of built-in potential in the device to dissociate photogenerated excitons effectively for self-powered operation. Our innovative approach in this study opens up an inventive direction for developing a cost-effective heterojunction-free self-powered photodetector.

I. INTRODUCTION

Photodetectors are basically a broad segment of optoelectronic devices for detecting light or photons efficiently. They have huge potential for use in many applications, such as in optical communication, medical diagnosis, imaging, safety and defense, and scientific research [1–3]. Photodetectors can be designed to operate over a wide range of wavelengths, from ultraviolet to infrared, and can extend applications further to environmental monitoring, spectroscopy, and biomedical imaging [4,5]. Photodetection largely depends on the active light-absorbing material's properties, and there are plenty of available materials to fabricate highly sensitive photodetectors. The choice of material depends on the targeted application. Traditional silicon (Si), indium gallium arsenide [(In, Ga)As], mercury cadmium telluride [(Hg, Cd)Te], germanium (Ge), and lead sulfide (PbS) are the most-explored materials for designing photodetectors with good sensitivity from the visible to long-wavelength-infrared regions [6–8]. Zinc oxide (ZnO) and gallium nitride (GaN) are known for detecting ultraviolet and blue light with high sensitivity [9]. Recently, various smart and advanced materials, including organic semiconductors, high-temperature superconductors, and two-dimensional (2D) layered

materials, were also utilized to show excellent photodetector performance with various application capabilities [10,11]. Moreover, there are many ongoing efforts to expand the scopes and capabilities of photodetectors by exploring different materials and device architectures.

In fact, a large variety of halide perovskite materials are now predominantly used to convert light into electricity because of their high optical absorption coefficient, tunable spectral response, long carrier diffusion length, and low effective mass of charge carriers [12]. Despite huge progress in perovskite photovoltaics, halide perovskite materials are also explored to design photodetectors with low-intensity-light detection capabilities. For example, hybrid methylammonium lead iodide (MAPbI$_3$), formamidinium lead iodide (FAPbI$_3$), and methylammonium lead bromide (MAPbBr$_3$) are used widely for photodetector design [5,13]. On the other hand, purely inorganic cesium lead bromide or iodide (CsPbBr$_3$ or CsPbI$_3$) are also explored to fabricate photodetectors because they have higher electron mobility [14,15]. Despite many advantages, perovskite photodetectors also face bottleneck issues in terms of stability, toxicity, and scalability. Furthermore, there is a need for photodetectors with a fast response time, ultralow dark current, and lower power consumption for areas like quantum communication, wearable technology, and Internet-of-things devices [16]. Therefore, self-powered photodetectors are becoming

---

*bikas@iisertvm.ac.in

familiar for enabling energy autonomy, but they require at least two semiconducting materials in combination to form a staggered-gap type-II heterojunction for dissociating photogenerated excitons easily and separating charge carriers [17,18]. Accordingly, many efforts have been made to address all the remaining challenges and unlock the full potential of photodetectors using halide perovskite materials [3,15,19].

Here, we demonstrate an innovative approach to fabricate an ultrasensitive self-powered photodetector with an ultralow dark current even at room temperature using an all-inorganic $CsPbBr_3$ monocrystal grown *in situ* directly over contact electrodes with asymmetric geometry. Interestingly, the origin of the self-powered operation without forming a conventional heterojunction is investigated theoretically using a back-to-back Schottky diode (BBS) model and experimentally at the nanoscale using the amplitude-modulated Kelvin-probe force microscopy (KPFM) technique. Both approaches clearly depict the asymmetry in the contact potential difference between the two contacts, which facilitates exciton dissociation and separation robustly. Our $Au/CsPbBr_3/Au$ photodetector demonstrates an attractive performance in self-powered mode for white light (as well as a green laser) with a light ON:OFF current (I_{ON}/I_{OFF}) ratio higher than 10^6, responsivity (R) of about 25 mA/W, specific detectivity (D^*) of 5.84×10^{12} Jones, and dark current of about 1 fA. The stability of the performance is found to be good over a period of 30 days. Systematic results analysis using the BBS model confirms the origin of the asymmetric barrier potentials at the electrode interfaces. Finally, we recorded the best performance of our self-powered $Au/CsPbBr_3/Au$ photodetector device using a low-intensity green laser with a wavelength of 532 nm in terms of responsivity (R) and specific detectivity (D^*) of about 2.0 A/W and 10^{14} Jones, respectively.

II. METHOD

A. Materials and chemicals

CsBr (99.999%), $PbBr_2$ (99.99%), dimethyl sulfoxide (DMSO, 99.9%), anhydrous acetonitrile (MeCN, 99.9%), hexamethyldisilazane (HMDS, 99%), hydrogen peroxide (H_2O_2, 30%), and ammonia solution (NH_4OH, 28–30%) were procured from Sigma Aldrich. Gold (Au, 99.999% purity) and titanium (Ti, 99.995% purity) were purchased from Kurt. J. Lesker, UK, to deposit metal electrodes for electrical contacts. Deionized (DI) water from a Milli-Q Direct 8 system with a resistivity of 18.2 $M\Omega$ cm was used for cleaning the substrates. All the chemicals were used as received without further purification.

B. Growth of $CsPbBr_3$ monocrystals

A precursor solution was prepared by dissolving 0.2-mM CsBr (42.56 mg) and 0.2-mM $PbBr_2$ (73.40 mg)

together in 1.0 ml of DMSO by stirring at a speed of 800 rpm and temperature of 40 °C for 24 h on a Heidolph magnetic stirrer hotplate. The precursor solution appeared transparent under laboratory light and green in color under UV-light illumination.

Meanwhile, borosilicate glass substrates were cut into pieces with dimensions of 15 (L) × 20 (W) mm^2 using a diamond-tip scriber and cleaned thoroughly following a standard protocol. The substrates were rinsed carefully using DI water as the final step of the cleaning procedure. Then, the substrates were dried by keeping inside a vacuum oven at temperature 80 °C for overnight. The cleaned and dried glass substrates were removed from the oven after reaching room temperature and immediately processed for surface protonating and deprotonating treatment after being treated in a UV-ozone cleaner (Holmarc, model HO-TH-UVO2) for 20 min at 95% emissivity to remove organic contaminants. To grow monocrystalline $CsPbBr_3$, the precursor should be placed over a deprotonated or hydrophilic substrate and then a protonated or hydrophobic substrate needs to be clipped from the top before soaking inside the antisolvent vapor, as illustrated in Fig. 1. For hydrophilic treatment, substrates were kept inside a mixture of H_2O_2-NH_4OH solution at a volume ratio of 1:3 for 3 h followed by rinsing with Milli-Q water and drying using a clean and dry air stream. After this hydrophilic treatment, substrates were ultrasonicated in Milli-Q water for 15 min then dried with hot air. For hydrophobic treatment, we performed HMDS treatment by spin coating a thin layer on the clean substrates at a speed of 4500 rpm for 45 s and annealing at 96 °C for 1 min on a hotplate before cooling to room temperature for further use.

We have grown monocrystalline $CsPbBr_3$ (MC CPB) crystals of dimensions as large as 100 (L) × 80 (W) $μm^2$ and thickness of about 2.5 μm using the antisolvent vapor-assisted crystallization (AVAC) technique [14,20]. Briefly, 50 μl of the precursor solution was drop cast over a hydrophilic glass substrate and immediately covered using a hydrophobic glass substrate of similar size followed by clipping with metal clippers to make the edges parallel. Then, these clipped substrates were placed inside a mouthless glass beaker together with a small glass petri dish containing 9 ml of MeCN as an antisolvent and the top of the beaker was sealed properly using another petri dish to avoid leakage or loss of MeCN vapor during crystal growth. Finally, the entire glass beaker system was placed over a hot plate at 40 °C for 16 h. During this crystal-growth period, the acetonitrile vapors diffused through the gap between the substrates and interacted with the precursor solution to initiate crystallization and this continued for the entire period, resulting in large-sized crystals.

C. Characterization of $CsPbBr_3$ monocrystals

Optical microscope images of the MC CPB crystal were recorded using an Olympus optical microscope (model
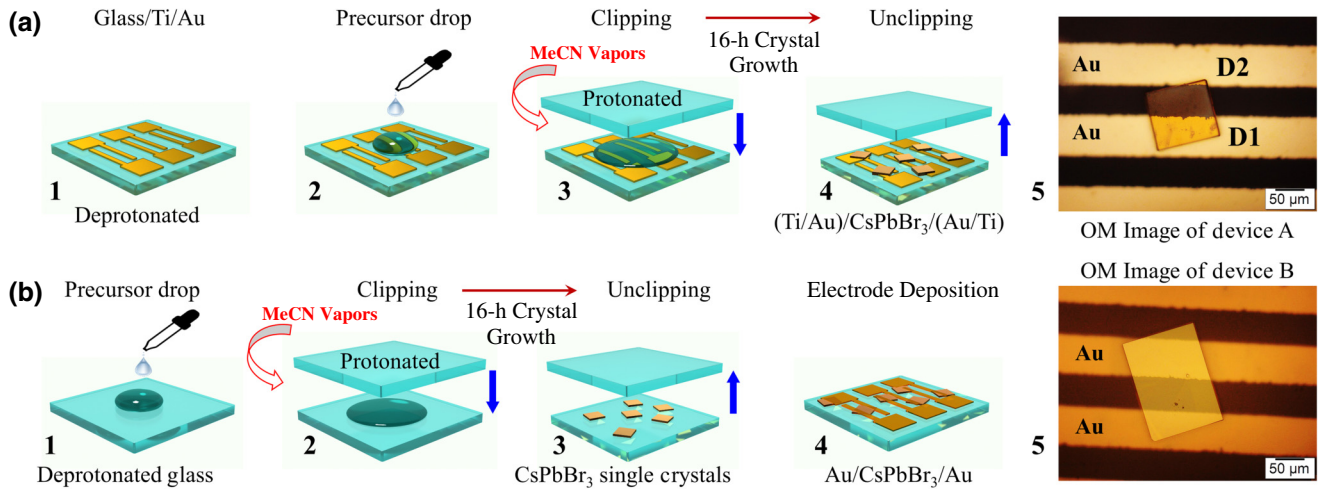
FIG. 1.   Schematics representing steps 1–4 of CsPbBr$_3$ monocrystal growth and device fabrication with OM images (step 5) of (a) device A and (b) device B.

BX53) to measure the dimension and shape more precisely. Surface topography and surface roughness of the crystal were analyzed by recording atomic force microscope (AFM) images using a JPK NanoWizard 4AF Bioscience AFM tool in tapping mode at the set point of 615 mV with a drive frequency and drive amplitude of 293.1 kHz and 80 mV, respectively. Electronic UV-visible absorption spectra were recorded using a PerkinElmer Lambda 950 UV/Vis/NIR spectrophotometer after calibration with the blank glass substrates. The thickness of the MC CPB crystal was estimated using a KLA Tencor D-600 profilometer at a scan speed of 30 μm/s. The x-ray diffraction spectrum of the MC CPB crystal was recorded using the Bruker-D8 Advance powder XRD tool in steps of 0.02°. Scanning electron microscopy (SEM) images and energy-dispersive x-ray spectroscopy (EDS) data were collected using an FEI-NOVA NANOSEM 450 SEM system fitted an with EDS system powered by GATAN APEX software for data collection and analysis.

D. Two-terminal planar device fabrication

This work involves two different types of devices: devices A and B. For device A (Au/MC CPB$_{post}$/Au), we deposited 50-nm-thick Au electrodes on the cleaned substrate before initiating the crystal-growth process with a 5-nm-thick titanium (Ti) adhesive layer for Au. For device B (Au/MC CPB$_{pre}$/Au), we grew the MC CPB crystal first and deposited 50-nm-thick gold (Au) electrodes later using electron-beam (e-beam) vacuum evaporation techniques through a metal shadow mask to complete the device fabrication process. We used a high-density interdigitated metal shadow mask with a 50-μm finger gap procured from Ossila Ltd, UK. For the e-beam evaporation of metal electrodes, we used a PRO Line PVD 75

high-vacuum deposition system procured from the Kurt J. Lesker Company, UK.

E. Optoelectronic measurements using white light and a green laser

Current-voltage (I-V) characteristics, both dc and temporal, under dark and light illumination for both device variants were determined inside a Janis UHV ST-500 micromanipulated probe station by directing light through the top quartz window at a chamber pressure of about 3×10^{-4} mbar for all cases, except a control experiment under ambient pressure. Devices were connected using gold-coated tungsten probes with a tip diameter of 25 μm. A Keithley 4200 SCS parameter analyzer containing three medium-powered source measuring units and a pulse measuring unit assembled via two remote preamplifiers was used to record all optoelectronic results. Low-noise triaxial cables were used to establish communication between devices and the 4200-SCS system. Photoresponses of the devices were studied using a Dolan-Jenner Fiber Lite white MI-LED B1 high-intensity illuminator with an intensity variation option from 10 to 100%. The intensities of white light were calibrated by using a Digital Luxmeter TES 1332A instrument. All pump-probe temporal responses were recorded by chopping the light manually. A diode laser procured from Holmarc Optomechatronics Pvt. Ltd. with specifications like $\lambda = 532$ nm, maximum output power of 5 mW, and 6.5 mm spot size was used to study the photoresponse of the device at low intensities. The intensity of the laser beam reaching the device was varied by using a home made set up consisting of a polarizer and an analyzer, and corresponding intensities were calibrated using a Luxmeter TES 1332A instrument.

F. Kelvin-probe force microscopy

A Park Systems NX7 atomic force microscope was used for AFM and KPFM characterization. KPFM measurements were performed using a silicon cantilever with a Cr/Pt collated tip (ElectriMulti75-G, Park System) with a probe radius of approximately 25 nm and a spring constant of around 3 N m^{-1}, with a 29.9-nm lift scan height. The contact resistance of the tip was 300 Ω and it had a resonance frequency of 75 kHz.

III. RESULTS AND DISCUSSION

A. Growth of CsPbBr$_3$ monocrystals and planar device fabrication

Despite the huge variety of photodetector devices, our approach remains very simple, and it is cheaper for others to reproduce the results easily with minimal facilities. Particularly, we fabricated CsPbBr$_3$ monocrystal photodetector devices with a planar structure of two different variants, devices A and B, as illustrated schematically in Fig. 1. For device A, we have grown large-sized CsPbBr$_3$ monocrystals *in situ* over glass substrates with prepatterned electrodes using the AVAC technique following steps 1–4 depicted in Fig. 1(a) [14]. Step 5 of Fig. 1(a) shows an optical microscope (OM) image of device A with a structure of Au/CsPbBr$_3$/Au, which is marked with D1 and D2 for the two different electrode geometries. It is evident that the D1 contact is larger than D2. Figure 1(b) shows steps 1–4 for the fabrication of device B, in which Au electrodes were deposited after growing the crystal, and step 5 shows the OM image of the final device. Despite differences in electrode geometries and crystal sizes, the channels remain constant for both devices.

B. Characterization of CsPbBr$_3$ monocrystal samples

Then we used various experimental techniques to identify the dimensions, surface roughness, optical band gap, crystallinity, and stoichiometry of the MC CPB samples. Figure 2(a) shows an image of MC CPB with dimensions of about 100 μm^2 for a growth time of 16 h. The thickness of MC CPB is measured to be about 2.5 μm using a profilometer [Fig. 2(b)]. The tapping-mode AFM topography image confirms the ultrasmooth surface of the CPB monocrystal [Fig. 2(c)], which reflects the rms area and line roughnesses of about 0.3 and 0.2 nm, respectively. Figure 2(d) shows a line profile extracted across the white line marked on the AFM topography, which again confirms the ultrasmooth surface. High-quality MC CPB growth is further supported by the SEM image [see Fig. S1(a) within the Supplemental Material [41]] in addition to the AFM analysis. Figure 2(e) shows the electronic UV-vis absorption spectrum displaying a peak at 522 nm and the sharp increase of absorption reflects the presence of a direct band gap. This indicates a direct band gap of 2.37 eV, which

is well supported by previously reported results [21,22]. The x-ray diffraction pattern in Fig. 2(f) shows four distinct peaks for the (002), (110), (004), and (220) lattice planes, which are consistent with the ICDD PDF No 04-014-9676 (see Fig. S2 within the Supplemental Material [41]) reference for the CsPbBr$_3$ orthorhombic phase with the *Pnma* space group and confirms no trace of any tetragonal and cubic phases [14]. The stoichiometric composition of the CPB sample is identified by recording the EDS-based atomic percentage and elemental mapping images of Cs, Pb, and Br with the overlaid mapping image for the same crystal, as shown in Figs. S1(b)–S1(f) within the Supplemental Material [41], respectively.

C. Optoelectronic characterization of CsPbBr$_3$ monocrystal devices

Next, we focused on probing the performance of our Au/CsPbBr$_3$/Au photodetector (PD) devices A and B using white light, as demonstrated schematically in Figs. 3(a) and 3(b), respectively. Particularly, the CsPbBr$_3$ monocrystal is grown on a substrate with prepatterned metal electrodes in the case of device A, which is exactly the opposite in case of device B (electrodes deposited after growing the crystal). Figures 3(c) and 3(d) show the current-voltage (*I-V*) characteristics of devices A and B, respectively, by sweeping the bias voltage back and forth between ±1.0 V in the dark and under light of intensity 15.49 mW/cm^2. Interestingly, device A shows a better photoresponse in terms of a higher light ON:OFF current ratio (3×10^5) at 1.0 V and a very low dark current of about 1 fA with no bias (0 V) at room temperature (25 °C). However, device B depicts a I_{light}/I_{dark} ratio about 1 order of magnitude lower with a much higher dark current (I_{dark}), indicating a poor PD performance compared with device A [19,23]. However, the dark current for both devices exhibited a hysteresis while sweeping the applied bias voltage back and forth. In halide perovskites, electrical conduction is contributed to by both charge carriers (electrons and holes) trapping-detrapping at the defect sites and ion migration. The activation energy of halide ions in a halide perovskite primarily has a meagre value, and it is about 28 meV for Br-ion motion in CsPbBr$_3$. Therefore, a room-temperature energy of about 26 meV, along with the applied bias voltage, is enough for the motion of Br ions in the crystal and to produce a hysteresis in the dark current [24]. The hysteresis is found to be more prominent for device B because of the additional contribution from interfacial defects. This hysteresis is suppressed under light illumination as the photogenerated carriers dominate.

Despite having similar device architectures, the crystal grown *in situ* directly over the prepatterned electrodes in device A results in a better performance due to forming cleaner and defect-free Au/CPB interfaces. Further investigation reveals a nonzero current (I_{SC}) at 0 V (applied
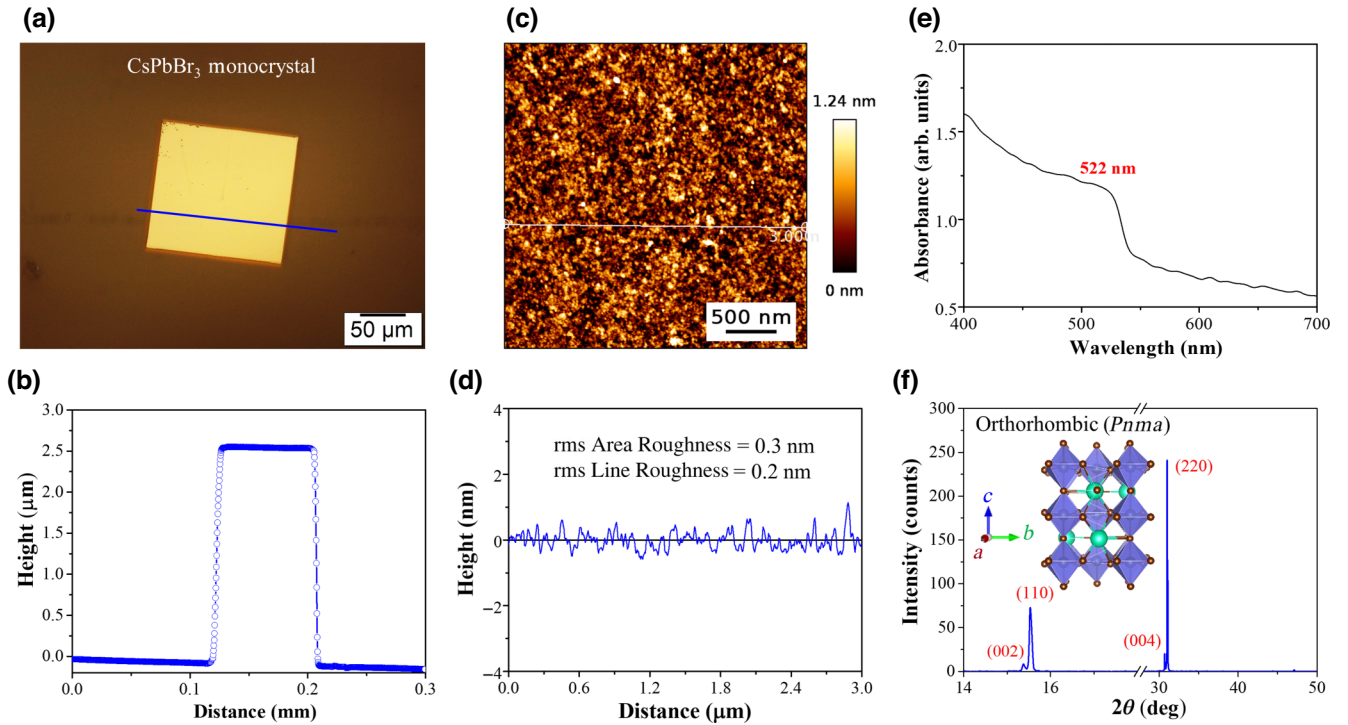
FIG. 2.   Characterization of *in situ* grown CsPbBr$_3$ monocrystal sample: (a) optical microscopy image, (b) profilometer thickness profile recorded along the blue line in (a), (c) AFM surface topography image in tapping mode, (d) a line profile traced along the white line, (e) UV-vis absorption spectrum, and (f) powder x-ray diffraction pattern. Inset, orthorhombic crystal structure of CsPbBr$_3$ with space group *Pnma*.

no bias) for device A, which needs an additional voltage (V_{OC}) to make it zero. In fact, this is similar to the photovoltaic response and useful for operating photodetector device A in self-powered mode [Fig. 3(e)]. For an incident light intensity of 15.5 mW/cm^2, I_{SC} and V_{OC} were recorded to be about 9.1 nA and 84 mV, respectively. However, PD device B does not show any self-powered nature, as can be seen from the enlarged *I-V* characteristics near the origin [Fig. 3(f)]. This performance anomaly between devices A and B actually originates from the difference in the device fabrication steps. It is already reported that evaporated metal electrodes show the Fermi-level pinning effect, which is dominating in device B to suppress the self-powered nature [25–27]. Further investigation was conducted to explore the impact of the asymmetric contact length and area on the self-powered operation of device A. Interestingly, it is primarily observed that the larger value of the D1:D2 contact-area ratio mostly dominates to show a higher V_{OC}, as demonstrated in Fig. S3 within the Supplemental Material [41]. However, this requires further systematic investigation and can be considered our next milestone [28]. Next, we recorded the temporal current responses for both devices by switching the light ON and OFF periodically under biased conditions (+1.0 V), as illustrated in Figs. S4(a) and S4(b) within the Supplemental Material [41], respectively. Particularly, device A shows a

very sharp rise and fall of the photocurrent due to it having defect-free interfaces [29]. Most significantly, the photovoltage in device A originates from the asymmetric contact geometry, despite the use of symmetric (gold) metal electrodes. We also tested device A using a green laser of varying incident power densities (12–245.1 μW/cm^2) and achieved an I_{light}/I_{dark} ratio as high as 10^5, as depicted in Fig. S5(a) within the Supplemental Material [41].

D. Self-powered photodetector performance

The above findings led us to investigate the performance in self-powered mode and the working principle behind it for device A systematically. Figure 4(a) shows a temporal current-response characteristic with no applied bias or self-power mode under incident light switching ON and OFF periodically with a power (P_{in}) density of 15.5 mW/cm^2. A similar test for device B results in a very weak self-powered response with rapid photocurrent decay, which is highlighted by comparing the linear photoresponse plots of devices A and B, as illustrated in Figs. S6(a) and S6(b) within the Supplemental Material [41], respectively. It is now confirmed that there is a very weak built-in potential to dissociate photogenerated excitons in device B due to the presence of the dominating Fermi-level pinning effect [27,30,31]. Interestingly, device A shows a dark current
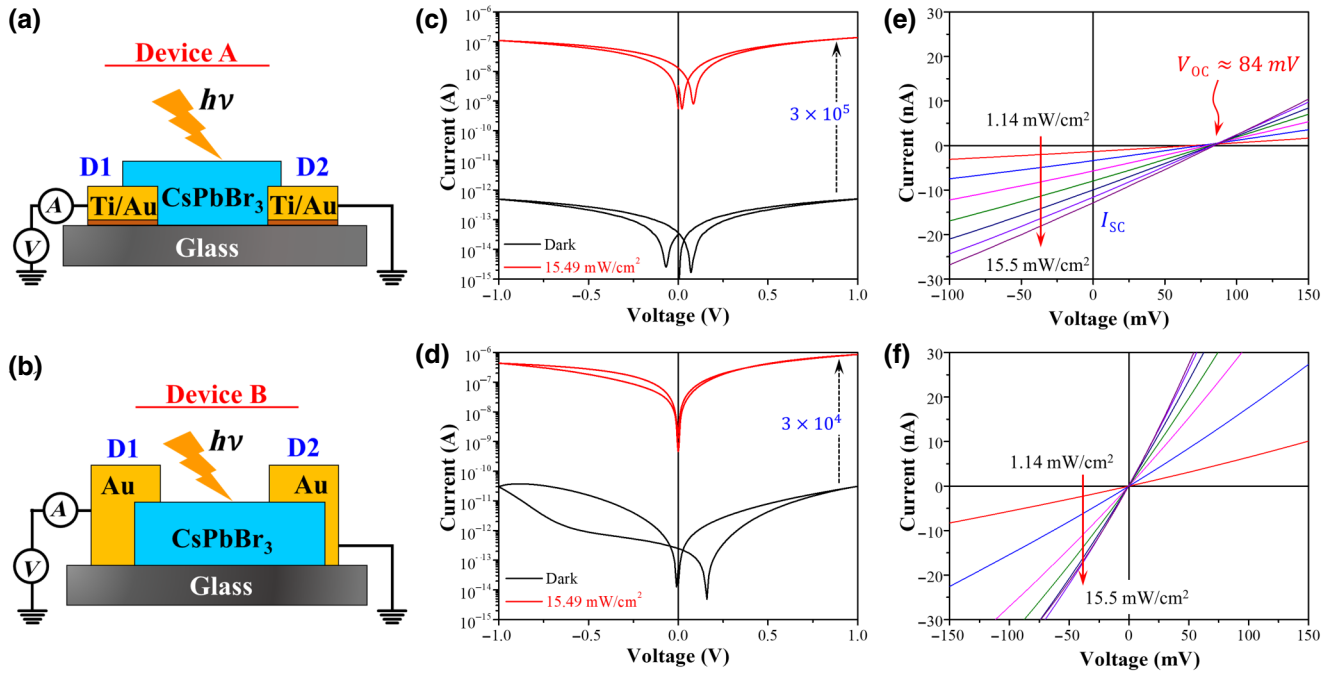
FIG. 3. Optoelectronic characterization of $Au/CsPbBr_3/Au$ devices A and B. (a),(b) Schematics of devices A and B, respectively, with asymmetric electrode geometries depicting the sequence of electrode deposition and monocrystal growth. (c),(d) Current-voltage (*I*-*V*) characteristics in the dark and under white light for devices A and B, respectively. (e),(f) Enlarged plots of *I*-*V* curves on a linear scale with varying light intensities near the origin for devices A and B, respectively.

(I_{dark}) of about 15 fA at 25 °C. Such a low I_{dark} depicts the capability of our $CsPbBr_3$ PD device to detect very-low-intensity light for the clean and interfacial-defect-free *in situ* Au/CPB interfaces [32]. Further investigation reveals a minimum I_{dark} of about 1 fA, as recorded consistently for device A in self-powered mode using a compliance current of 10 pA at room temperature (Fig. S7 within the Supplemental Material [41]). In particular, we achieved a short-circuit current (I_{SC}) of about 9.1 nA for a light intensity of 15.5 mW/cm^2, which resulted in a I_{light}/I_{dark} ratio of 6×10^5 for $I_{dark} = 15$ fA and about 10^7 for the 1-fA dark current; the performance appears to be exceptionally good [18]. We have varied the incident light power to record temporal photoresponses at 0.0 V applied bias, as shown in Fig. S8 within the Supplemental Material [41], and extracted light-power-dependent photocurrents ($I_{ph} = I_{SC} - I_{dark}$), which showed almost linear dependency on the incident light power, as depicted in Fig. 4(b). It follows the relation $I_{ph} \propto P_{in}^{\gamma}$ with a γ value of 0.906, indicating defect-free interfaces and minimal charge-carrier recombination. Conventionally, γ has a maximum value of one for defect-free interfaces of a PD device; otherwise, it has a lower value [33]. In fact, the γ value is about 1.01 when we use a green laser with a low power density [Fig. S5(b) within the Supplemental Material [41]]. Furthermore, we have recorded the temporal response by

varying the incident light power (P_{in}) step by step; this displayed a nice linear photocurrent enhancement, as shown in Fig. 4(c) in self-powered mode. Next, we probed the response speed by recording a temporal current response for a light pulse of 10 s in duration, as shown in Fig. 4(d), which displayed rise (τ_{rise}) and fall times (τ_{fall}) of about 230 and 60 ms, respectively.

In practice, the low-light-detection capability or sensitivity of a PD is mostly indicated by the higher responsivity (*R*) and specific detectivity (*D**) values. The responsivity (*R*) of our device A is estimated by

$$R = \frac{I_{ph}}{P_{in}} = \frac{I_{SC} - I_{dark}}{P_{in}},$$

for different P_{in} [Fig. 4(e)], with the *R* value recorded after 30 days in self-powered mode. Interestingly, we achieved an *R* of about 20 mA/W in self-powered mode, which was found to be quite stable over a period of 30 days. To estimate the specific detectivity for different incident light powers, we have used the formula $D^* = \left(\sqrt{AR}\right)/\sqrt{2eI_{dark}}$, where *A* and *e* represent the effective area of the device (2854 μm^2) and electronic charge [Fig. 4(f)]. It indicates that a higher *D** value can be achieved for a low I_{dark}. Moreover, I_{dark} depends on thermally generated carriers in the photoactive layer and on the
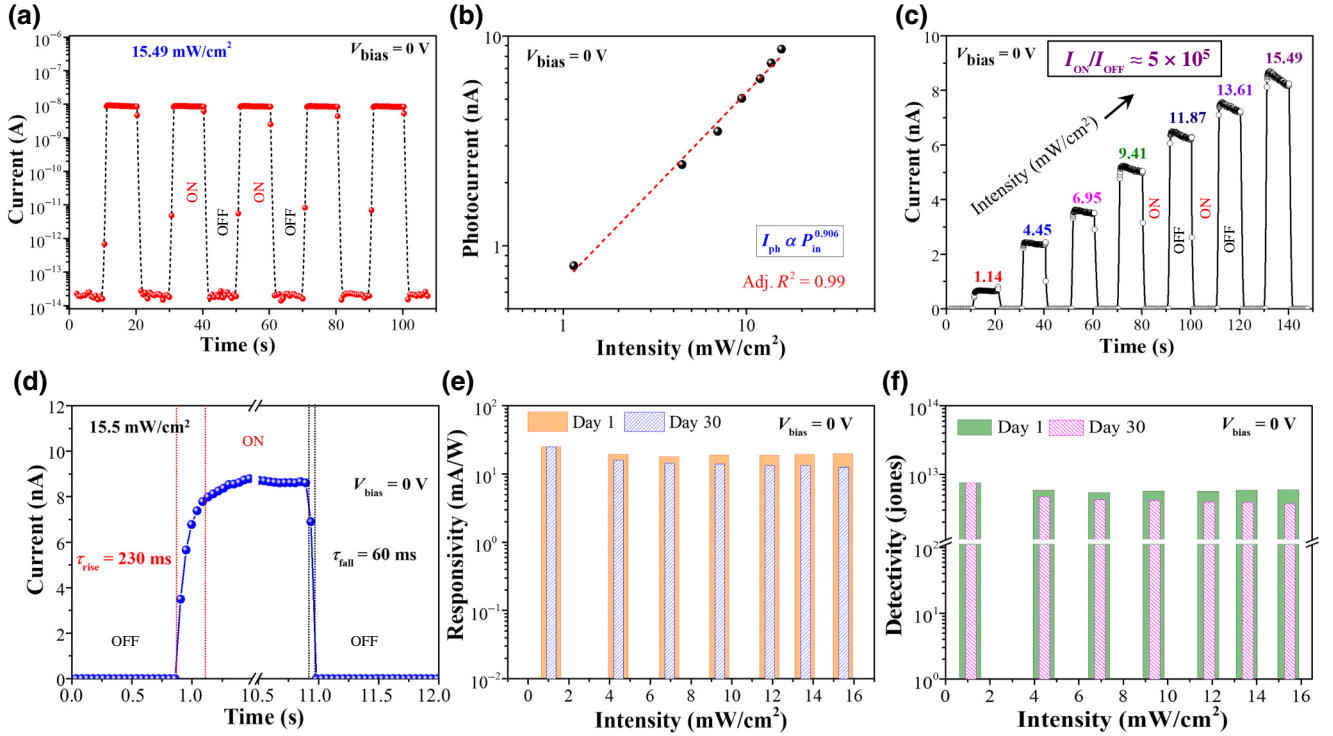
FIG. 4. Self-powered photodetector performance of device A. (a) Temporal photoresponse, (b) variation of photocurrent with incident light intensity, (c) temporal response under increasing incident light intensity, (d) photoresponse speed at an incident light intensity of 15.5 mW/cm^2, (e),(f) responsivity (R) and specific detectivity (D^*), respectively, at different incident light intensities recorded on day 1 (bars of solid colors) and after 30 days (bars of patterned lines).

active area and temperature. Normally, displaying a higher dark current is a major drawback for any photodetector. Hence, we believe that the I_{dark} of 1 fA recorded at room temperature for our all-inorganic MC CPB perovskite photodetector is a remarkable achievement. On average, the D^* value is found to be as high as 7.35×10^{12} Jones under white-light illumination, which also remains almost invariant over a period of 30 days [Fig. 4(f)]. This strongly reflects the high-performance stability of our CsPbBr$_3$ perovskite photodetector. To highlight the reproducibility, we have arbitrarily picked and characterized 11 different devices fabricated in two different batches, as depicted in Figs. S9(a)–S9(c) within the Supplemental Material [41] in terms of I_{light}/I_{dark} ratio, responsivity (R), and specific detectivity (D^*), respectively. Interestingly, the responsivity of 20 A/W and detectivity of 10^{14} Jones were achieved under 1.0-V applied bias using a green laser of low power density, which were found to be about 2 A/W and 10^{14} Jones in self-powered mode, respectively, as illustrated in Figs. S5(c) and S5(d) within the Supplemental Material [41], respectively. The performance of our self-powered Au/CPB/Au PD device is compared with the results reported for similar types of devices, as shown in Table S1 within the Supplemental Material [41]; this reflects that the results for our device are promising.

E. Origin of self-powered operation in the absence of a semiconductor heterojunction

To investigate the working principle of our MC CPB photodetector in self-powered mode, we have considered the BBS circuit model from the analogy of asymmetric contact geometries D1 (large) and D2 (small) connected with a resistor R as illustrated schematically in the lower panel of Fig. 5(a) comparing with the actual device architecture (upper panel) [34]. As per this BBS model, the applied bias voltage, V_{bias}, can be expressed by Eq. (1), which is illustrated step by step in Sec. S1 within the Supplemental Material [35,41].

$$V_{bias} = \frac{1}{\alpha_1} \ln\left[1 + \frac{I}{I_{01}}\right] - \frac{1}{\alpha_2} \ln\left[1 - \frac{I}{I_{02}}\right] + IR, \quad (1)$$

where α_1 and α_2 represent constants, I_{01} and I_{02} represent reverse saturation currents for the respective contacts and $I =$ current in the circuit. Equation (1) is utilized to fit the I-V curve recorded in the dark, as shown in Fig. 5(b), and different device parameters are extracted, including the Schottky barrier height for contacts D1 and D2 (see Sec. S1 and Table S2 within the Supplemental Material [41]). The series resistance, R, is found to be about 1.8×10^{12} Ω. In general, the ideality factor of unity (1) resembles the sole
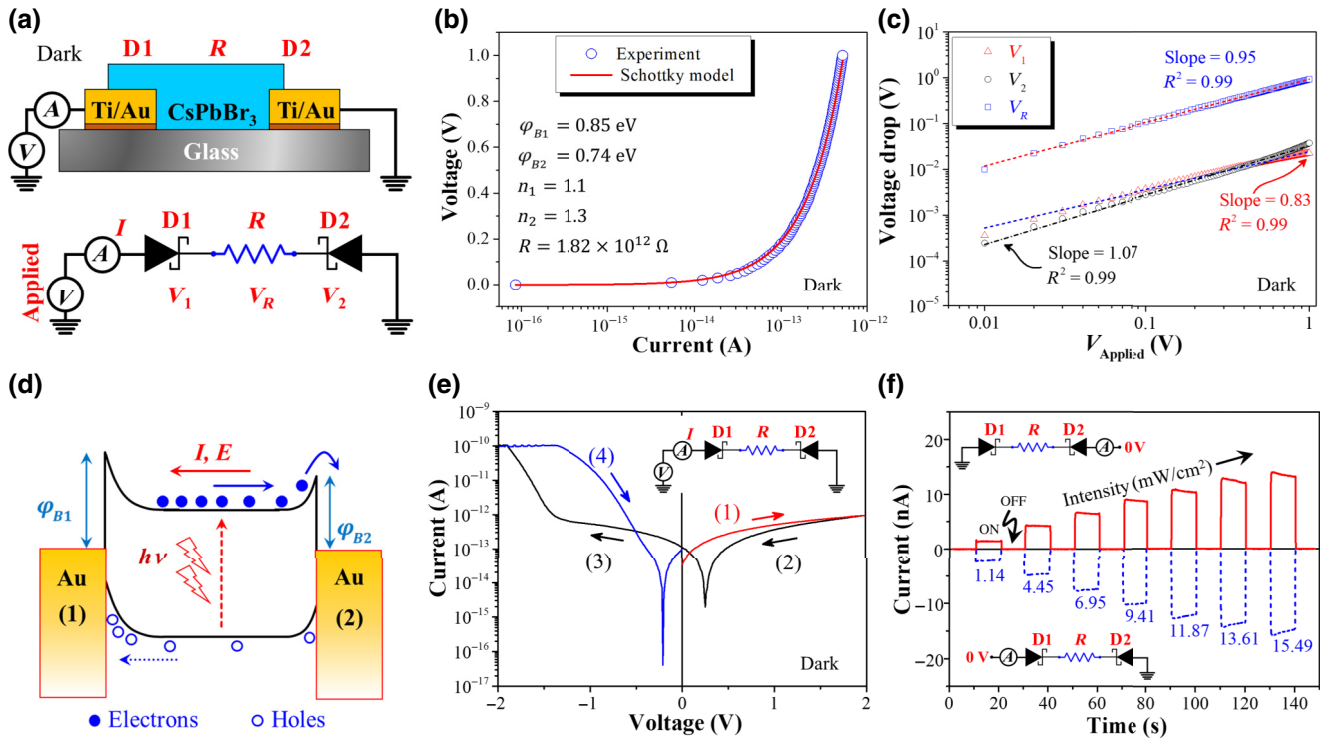
FIG. 5. Operation principle of device A. (a) Cross-sectional view of the device schematic (top panel) marked with Schottky contacts D1 and D2 connected by resistor R and the corresponding equivalent circuit (bottom panel) considering the BBS model. (b) Curve fitting and extracted parameters using the dark current for positive-bias polarity. (c) Voltage-drop profile across contacts D1, D2, and connecting resistor R. (d) Schematic representation of the energy-band diagram with an asymmetric Schottky barrier height for driving the device in self-power mode. (e) I-V characteristics recorded in a loop by sweeping voltage between ± 2.0 V under dark. Inset, BBS circuit for this test. (f) Self-powered temporal photoresponse recorded by interchanging sensing and electrical grounding connections. Top inset, BBS equivalent circuit with contact D1 grounded. Bottom inset, BBS equivalent circuit with contact D2 grounded.

thermionic emission and higher values reflect contributions from field-enhanced and thermally assisted tunneling [34]. Interestingly, the asymmetry in the Schottky barrier height is nicely supported by this BBS model for device A. The voltage drops across the components, like the D1 interface (V_1), the D2 interface (V_2), and resistor R (V_R), and the applied voltage nicely depicts a power-law dependence [Fig. 5(c)] with slopes close to unity. Furthermore, we have utilized the V_{OC} dependence of the incident light power (P_{in}) equation ($V_{OC} = (nkT/q) \ln(P_{in}) + C$, where n, k, T, q, and C represent the ideality factor, Boltzmann constant, temperature, electronic charge, and a constant, respectively) for a p-n junction solar cell and found the difference in ideality factors to be about 0.23, very close to the value resulting from the BBS model, as illustrated in Sec. S3 within the Supplemental material [41]. This again strongly resembles the correctness of the BBS model analysis results [33,36].

Based on extracting parameters using the BBS model, we have proposed an energy-band diagram to illustrate the self-powered operation of the photodetector [Fig. 5(d)]. It clearly depicts the asymmetry of the Schottky barrier height between contacts D1 and D2 originating from the

asymmetry of the contact electrode geometries. Furthermore, it is evident from the energy-band diagram that the photogenerated excitons dissociate easily in the presence of a built-in potential due to different contact potential barriers at the electrode interfaces and being collected by the electrodes to drive a current in the external circuit for self-powered operation. It also depicts that the holes does not face any barriers to reach the electrodes, but electrons do have a slight barrier at the small-contact-geometry electrode, which strongly resembles dominating hole conduction and would result in higher hole mobility, as reported earlier elsewhere [14]. Figure 5(e) shows the rectifying I-V characteristics recorded in a loop between applied bias voltages of ± 2.0 V, which strongly support the existence of an asymmetric potential barrier height between the contacts from the rectifying nature [36]. Interestingly, a prominent resistive switching is also observed with a large conductivity difference between the forward and backward sweep directions. This needs an in-depth study and could be the objective of another future project. Furthermore, we recorded temporal current responses by turning the light ON and OFF in self-powered mode just by interchanging the sensing ammeter and ground
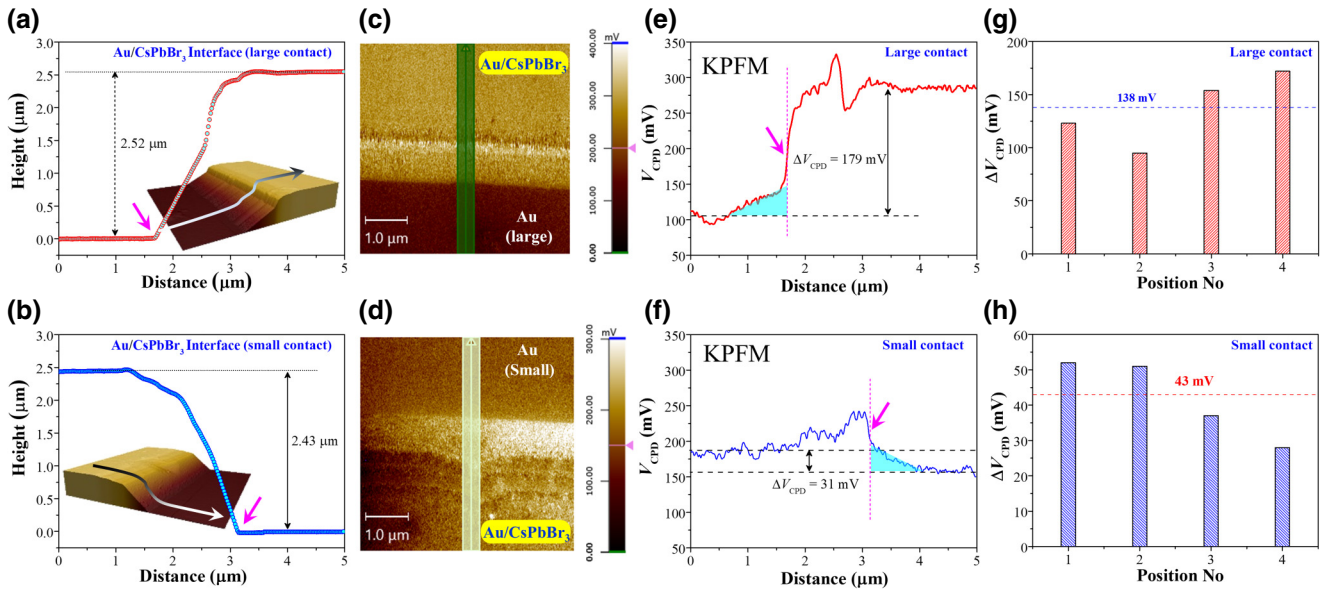
FIG. 6. (a),(b) AFM height profiles recorded at the large and small Au/CPB interfaces, respectively. Insets show the respective 3D AFM topography images with the scan direction. (c),(d) KPFM surface-potential maps for the AFM topography areas (a),(b) of Au/CPB interfaces, respectively. (e),(f) Average contact-potential difference (V_{CPD}) along the line with shaded region over (c),(d), respectively. (g),(h) Change in V_{CPD} measured for four different locations of large- and small-contact-area interfaces, respectively. Inclined pink-colored arrows indicate sharp interfaces of Au/CsPbBr$_3$.

connections, as demonstrated in the BBS circuit model and illustrated schematically by the inset models in Fig. 5(f), which depict exact flipping of the photocurrent polarity. This strongly supports a unidirectional flow of photocurrent and supports our proposed theoretical BBS model to operate the Au/CPB/Au PD in self-powered mode.

F. KPFM to probe the synergy between contact-area differences and self-powered PD operation

It is intriguing to probe the origin of the self-powered operation of the Au/CPB/Au PD device without having a conventional semiconductor type-II staggered heterojunction. Accordingly, we have utilized the KPFM technique to investigate the origin of the driving built-in potential, which dissociates the photogenerated excitons into electrons and holes. For that, we have selected an Au/CPB/Au device with asymmetric contact geometries and recorded the surface potential (contact potential difference, V_{CPD}) over an interfacial area of Au and Au/CBP for both contacts using the amplitude-modulated KPFM method under dark conditions. In general, the origin of V_{CPD} is calculated by $V_{CPD} = (\varphi_s - \varphi_t)/e$, where e, φ_s, and φ_t represent electronic charge and sample and AFM tip work functions, respectively [37]. Figures 6(a) and 6(b) represent the height profiles extracted along the line drawn over the respective three-dimensional (3D) AFM image (inset) of large and small Au/CPB contacts, respectively, which depict a thickness of the CPB crystal of about 2.5 μm; this is in good agreement with the profilometer thickness

data shown in Fig. 2(b). The respective surface-potential mapping images in Figs. 6(a) and 6(b) were recorded using a Cr/Pt-coated AFM tip in amplitude-modulated KPFM mode, as shown in Figs. 6(c) and 6(d), respectively; which are originated from the interfacial energy-level alignment [38]. Interestingly, the large Au/CPB contact resulted in a large change in contact potential difference (ΔV_{CPD}) and the small Au/CPB contact resulted in a small ΔV_{CPD} between Au and Au/CPB, which resulted from the extracted average line profile in Figs. 6(c) and 6(d), as illustrated in Figs. 6(e) and 6(f), respectively. Particularly, ΔV_{CPD} is found to be about 179 mV for the large contact and 31 mV for the smaller one; these values strongly support our previous analysis using the BBS model. After repeating similar tests at four different locations on each Au/CPB contact, the difference of V_{CPD} between the large and small contacts is found to be about 100 mV, which is the driving force to operate our Au/CPB/Au PD device in self-powered mode. Notably, the ΔV_{CPD} is found to be almost zero for both contacts of device B from the recorded KPFM results, as shown in Fig. S15 within the Supplemental Material [41], which again strongly supports our previous claim of Fermi-level pinning. Hence, the synergy between the difference in contact-area geometries and self-powered PD operation originated from the imbalance of ΔV_{CPD}.

The physical origin of the asymmetric Schottky barrier height could be explained using the line profiles extracted from the KPFM images of large and small contacts of our device A, as shown in Figs. 6(e) and 6(f), which show

a cyan-colored shaded region for the spatial variation of V_{CPD} or uncompensated electric field at the periphery of the metal contact. This actually suppresses the interfacial barrier height for a metal-semiconductor junction. It is also observed that this barrier-height suppression was found to be stronger for a smaller metal contact than a larger one, as observed from the KPFM results for our device A [39]. In fact, it is obvious that strain can develop at the electrode periphery in contact with the CsPbBr$_3$ crystal; this can be ascribed to the central displacements of Pb^{2+} cations and Br$^-$ anions in the highly distorted octahedral [PbBr$_6$]$^{4-}$ [40]. This strain could induce a paraelectric-to-ferroelectric transition in CsPbBr$_3$ at the periphery region of the metal contact with the CsPbBr$_3$ crystal or thin film, and this is reflected by the bright region in the KPFM-based surface-potential mapping images.

IV. CONCLUSION

We successfully demonstrated a high-performance self-powered photodetector using an all-inorganic CsPbBr$_3$ monocrystal grown *in situ* directly over prepatterned metal electrodes of asymmetric contact geometries with a device architecture of Au/CsPbBr$_3$/Au. The solution-based AVAC technique assisted in high-quality CsPbBr$_3$ monocrystal growth, as confirmed using various experimental techniques. The necessity for defect-free clean interfaces between the metal electrodes and MC CPB for an extremely low dark current at room temperature is established from the performance difference between two different device variants of similar structure prepared through different fabrication steps. Devices with the CsPbBr$_3$ crystal grown *in situ* over predeposited electrodes have only shown consistent high-performance self-powered operation with a dark current as low as 1 fA at room temperature; this is a benchmark achievement according to our perception. The robustness of the photodetector performance is verified in normal and self-powered modes under white light and a low-intensity green laser. The difference in contact geometries plays a vital role in the origin of the built-in potential to dissociate photogenerated excitons easily. The defect-free clean interfaces minimize the loss of carriers due to trapping and recombination; this is strongly supported by the experimental findings, including the recorded contact potential difference between electrodes using the KPFM method. This work reports the design of a staggered heterojunction-free self-powered photodetector using the MC CPB grown *in situ* as the photoactive layer. The BBS model is used to analyze our experimental findings and extract the device parameters, and the results nicely support our device results and working principle. Notably, the stability of the performance over a period of 30 days and high reproducibility among multiple devices fabricated in different batches make our approach technologically relevant to meet future

industrial demands. Overall, any semiconductor, including halide perovskites, could attract interest for the design of self-powered high-performance photodetectors with a similar device architecture to that proposed here, provided that the Fermi-level pinning effect could be suppressed by creating defect-free metal-semiconductor interfaces.

Data that support the findings of this study are available from the corresponding author upon reasonable request.

[1] R. D. Jansen-van Vuuren, A. Armin, A. K. Pandey, P. L. Burn, and P. Meredith, Organic photodiodes: The future of full color detection and image sensing, Adv. Mater. **28,** 4766 (2016).

[2] F. H. L. Koppens, T. Mueller, P. Avouris, A. C. Ferrari, M. S. Vitiello, and M. Polini, Photodetectors based on graphene, other two-dimensional materials and hybrid systems, Nat. Nanotechnol. **9,** 780 (2014).

[3] H. P. Wang, S. Y. Li, X. Y. Liu, Z. F. Shi, X. S. Fang, and J. H. He, Low-dimensional metal halide perovskite photodetectors, Adv. Mater. **33,** 2003309 (2021).

[4] C. H. Liu, Y. C. Chang, T. B. Norris, and Z. H. Zhong, Graphene photodetectors with ultra-broadband and high responsivity at room temperature, Nat. Nanotechnol. **9,** 273 (2014).

[5] J. Yan, Q. Zheng, S. P. Wang, Y. Z. Tian, W. Q. Gong, F. Gao, J. J. Qiu, L. Li, S. H. Yang, and M. S. Cao, Multi-functional organic-inorganic hybrid perovskite microcrystalline engineering and electromagnetic response switching multi-band devices, Adv. Mater. **35,** 2300015 (2023).

[6] G. Konstantatos, I. Howard, A. Fischer, S. Hoogland, J. Clifford, E. Klem, L. Levina, and E. H. Sargent, Ultrasensitive solution-cast quantum dot photodetectors, Nature **442,** 180 (2006).

[7] K. M. Sandhya and B. C. Das, Plasmonic hot carrier induced photosensitization of CdSe quantum dots: Role of phonons, J. Phys. Chem. C **124,** 12095 (2020).

[8] G. Q. Cao, F. Wang, M. Peng, X. M. Shao, B. Yang, W. D. Hu, X. Li, J. Chen, Y. B. Shan, P. S. Wu, *et al.*, Multicolor broadband and fast photodetector based on InGaAs-insulator-graphene hybrid heterostructure, Adv. Electron. Mater. **6,** 1901007 (2020).

[9] J. Li, X. Xi, S. Lin, Z. H. Ma, X. D. Li, and L. X. Zhao, Ultrahigh sensitivity graphene/nanoporous GaN ultraviolet photodetectors, ACS Appl. Mater. Interfaces **12**, 11965 (2020).

[10] I. Charaev, D. A. Bandurin, A. T. Bollinger, I. Y. Phinney, I. Drozdov, M. Colangelo, B. A. Butters, T. Taniguchi, K. Watanabe, X. He, *et al.*, Single-photon detection using high-temperature superconductors, Nat. Nanotechnol. **18**, 343 (2023).

[11] Y. X. Sun, G. Niu, W. Ren, X. J. Meng, J. Y. Zhao, W. B. Luo, Z. G. Ye, and Y. H. Xie, Hybrid system combining two-dimensional materials and ferroelectrics and its application in photodetection, ACS Nano **15**, 10982 (2021).

[12] J. K. Yan, H. J. Li, M. H. Aldamasy, C. Frasca, A. Abate, K. Zhao, and Y. Hu, Advances in the synthesis of halide perovskite single crystals for optoelectronic applications, Chem. Mater. **35**, 2683 (2023).

[13] K. Leng, I. Abdelwahab, I. Verzhbitskiy, M. Telychko, L. Q. Chu, W. Fu, X. Chi, N. Guo, Z. H. Chen, Z. X. Chen, *et al.*, Molecularly thin two-dimensional hybrid perovskites with tunable optoelectronic properties due to reversible surface relaxation, Nat. Mater. **17**, 908 (2018).

[14] Z. Yang, Q. Xu, X. D. Wang, J. F. Lu, H. Wang, F. T. Li, L. Zhang, G. F. Hu, and C. F. Pan, Large and ultrastable all-inorganic CsPbBr$_3$ monocrystalline films: Low-temperature growth and application for high-performance photodetectors, Adv. Mater. **30**, 1802110 (2018).

[15] Z. Q. Li, Z. L. Li, Z. F. Shi, and X. S. Fang, Facet-dependent, fast response, and broadband photodetector based on highly stable all-inorganic CsCu$_2$I$_3$ single crystal with 1D electronic structure, Adv. Funct. Mater. **30**, 2002634 (2020).

[16] Y. Xu, R. Li, S. Bai, Y. Li, Z. Jia, Y. Yang, E. Cui, F. Yao, D. Wang, C. Lei, *et al.*, Chalcogenide-based narrowband photodetectors for imaging and light communication, Adv. Funct. Mater. **33**, 2212523 (2023).

[17] W. Tian, Y. D. Wang, L. Chen, and L. Li, Self-powered nanoscale photodetectors, Small **13**, 1701848 (2017).

[18] K. X. Chen, X. L. Zhang, P. A. Chen, J. Guo, M. He, Y. Q. Chen, X. C. Qiu, Y. Liu, H. J. Chen, Z. B. Zeng, *et al.*, Solution-processed CsPbBr$_3$ quantum dots/organic semiconductor planar heterojunctions for high-performance photodetectors, Adv. Sci. **9**, 2105856 (2022).

[19] F. T. Chen, C. Q. Li, C. Y. Shang, K. Y. Wang, Q. Huang, Q. Q. Zhao, H. L. Zhu, and J. X. Ding, Ultrafast response of centimeter scale thin CsPbBr$_3$ single crystal film photodetector for optical communication, Small **18**, 2203565 (2022).

[20] Y. Rakita, N. Kedem, S. Gupta, A. Sadhanala, V. Kalchenko, M. L. Bohm, M. Kulbak, R. H. Friend, D. Cahen, and G. Hodes, Low-temperature solution-grown CsPbBr$_3$ single crystals and their characterization, Cryst. Growth Des. **16**, 5717 (2016).

[21] Y. F. Wang, F. Yang, X. Z. Li, F. Ru, P. Liu, L. Wang, W. Ji, J. Xia, and X. M. Meng, Epitaxial growth of large-scale orthorhombic CsPbBr$_3$ perovskite thin films with anisotropic photoresponse property, Adv. Funct. Mater. **29**, 1904913 (2019).

[22] M. I. Saidaminov, M. A. Haque, J. Almutlaq, S. Sarmah, X. H. Miao, R. Begum, A. A. Zhumekenov, I. Dursun, N. Cho, B. Murali, *et al.*, Inorganic lead halide perovskite single crystals: Phase-selective low-temperature growth, carrier transport properties, and self-powered photodetection, Adv. Opt. Mater. **5**, 1600704 (2017).

[23] E. Oksenberg, E. Sanders, R. Popovitz-Biro, L. Houben, and E. Joselevich, Surface-guided CsPbBr$_3$ perovskite nanowires on flat and faceted sapphire with size-dependent photoluminescence and fast photoconductive response, Nano Lett. **18**, 424 (2018).

[24] J. Cai, T. Zhao, M. M. Chen, J. Y. Su, X. M. Shen, Y. Liu, and D. W. Cao, Ion migration in the all-inorganic perovskite CsPbBr$_3$ and its impacts on photodetection, J. Phys. Chem. C **126**, 10007 (2022).

[25] M. J. Dai, H. Y. Chen, R. Feng, W. Feng, Y. X. Hu, H. H. Yang, G. B. Liu, X. S. Chen, J. Zhang, C. Y. Xu, *et al.*, A dual-band multilayer InSe self-powered photodetector with high performance induced by surface plasmon resonance and asymmetric Schottky junction, ACS Nano **12**, 8739 (2018).

[26] C. J. Zhou, S. Raju, B. Li, M. Chan, Y. Chai, and C. Y. Yang, Self-driven metal-semiconductor-metal WSe$_2$ photodetector with asymmetric contact geometries, Adv. Funct. Mater. **28**, 1802954 (2018).

[27] K. Hong, K. C. Kwon, K. S. Choi, Q. Van Le, S. J. Kim, J. S. Han, J. M. Suh, S. Y. Kim, C. M. Sutter-Fella, and H. W. Jang, Strong Fermi-level pinning at metal contacts to halide perovskites, J. Mater. Chem. C **9**, 15212 (2021).

[28] J. T. Lu, Z. Q. Zheng, J. D. Yao, W. Gao, Y. Xiao, M. L. Zhang, and J. B. Li, An asymmetric contact-induced self-powered 2D In$_2$S$_3$ photodetector towards high-sensitivity and fast-response, Nanoscale **12**, 7196 (2020).

[29] Y. Zhao, C. L. Li, and L. Shen, Recent advances on organic-inorganic hybrid perovskite photodetectors with fast response, Infomat **1**, 164 (2019).

[30] C. Kim, I. Moon, D. Lee, M. S. Choi, F. Ahmed, S. Nam, Y. Cho, H. J. Shin, S. Park, and W. J. Yoo, Fermi level pinning at electrical metal contacts of monolayer molybdenum dichalcogenides, ACS Nano **11**, 1588 (2017).

[31] L. Li, Y. Chen, C. Cai, P. Ma, H. Ji, and G. Zou, Single crystal halide perovskite film for nonlinear resistive memory with ultrahigh switching ratio, Small **18**, 2103881 (2022).

[32] K. Y. Zhao, J. X. Zou, F. M. Huang, C. F. Gao, X. Wang, W. W. Li, W. Tian, Y. F. Lin, Z. G. Hu, and J. H. Chu, Asymmetric Au electrodes-induced self-powered organic-inorganic perovskite photodetectors, IEEE Trans. Electron Devices **68**, 1149 (2021).

[33] N. K. Krishnan, A. Sreedharan, S. Sagar, L. T. Manamel, A. Mukherjee, and B. C. Das, Self-powered broadband photodetection of copper phthalocyanine by enhancing photogating effect with monolayer MoS$_2$ flakes, Appl. Surf. Sci. **568**, 150818 (2021).

[34] G. Bhattacharya and A. Venimadhav, An alternative approach to extract diode parameters from metal-semiconductor-metal asymmetric Schottky diodes, J. Phys. D: Appl. Phys. **55**, 435101 (2022).

[35] A. Grillo and A. Di Bartolomeo, A current-voltage model for double Schottky barrier devices, Adv. Electron. Mater. **7**, 2000979 (2021).

[36] A. Di Bartolomeo, A. Grillo, F. Urban, L. Iemmo, F. Giubileo, G. Luongo, G. Amato, L. Croin, L. F. Sun, S. J. Liang,

et al., Asymmetric Schottky contacts in bilayer MoS_2 field effect transistors, Adv. Funct. Mater. **28,** 1800657 (2018).

[37] A. Bera, S. Paramanik, A. Maiti, and A. J. Pal, Energy landscape in silver-bismuth-iodide rudorffites: Combining scanning tunneling spectroscopy and Kelvin probe force microscopy, Phys. Rev. Mater. **5,** 095404 (2021).

[38] P. Y. Qiao, J. Xia, X. Z. Li, Y. Y. Li, J. Y. Cao, Z. S. Zhang, H. Lu, Q. Meng, J. T. Li, and X. M. Meng, Epitaxial van der Waals contacts of 2D $TaSe_2$-WSe_2 metal–semiconductor heterostructures, Nanoscale **15,** 17036 (2023).

[39] H. Efeoglu, A. Turut, and M. Gül, An experimental study: Dependence of Schottky diode parameters on Schottky contact area size, Opt. Mater. **142,** 114038 (2023).

[40] X. J. Gao, Q. Wang, Y. Zhang, C. L. Cui, N. Sui, X. C. Chi, H. Z. Zhang, Q. Zhou, Y. J. Bao, and Y. H. Wang, Pressure effects on optoelectronic properties of $CsPbBr_3$ nanocrystals, J. Phys. Chem. C **124,** 11239 (2020).

[41] See the Supplemental Material at http://link.aps.org/supple mental/10.1103/PhysRevApplied.21.044015 for the morphology and elemental stoichiometry of MC CPB using SEM and EDS, powder x-ray diffraction pattern of MC CPB, biased temporal photoresponse for both devices, PD performance using a green laser, temporal response of device A in self-power mode with a current compliance of 10 pA, statistical PD performance data taken for 11 different arbitrarily picked devices of type A, back-to-back Schottky diode analysis related *I-V* curves for the individual interfaces, photodetector of aluminum contact electrodes with a structure of Al/MC CPB/Al, temporal photoresponses at different incident white-light intensities (1.14–15.5 mW/cm^2) for device A in self-powered mode, performance comparison table, BBS model details, performance-related discussions using a green laser, and supplemental references.